Adaptive track estimation on a radar array system for space surveillance

M. F. Montaruli[a], L. Facchini[a], P. Di Lizia[a], M. Massari[a], G. Pupillo[b], G. Bianchi[b], G. Naldi[b]

[a]*Department of Aerospace Science and Technology, Politecnico di Milano Via G. La Masa 34, 20156, Milan, Italy*
[b]*Istituto di Radioastronomia, Istituto Nazionale di Astrofisica Via P. Gobetti 101, 40129, Bologna, Italy*

Abstract

The increasing population of resident space objects is currently fostering many Space Surveillance and Tracking (SST) initiatives, which are based on the use of ground sensors. Italy contributes to the European SST Support Framework with the BIstatic RAdar for LEo Survey (BIRALES). Orbit determination from BIRALES observations relies on the estimation of the angular profiles of the object crossing the sensor field of view by processing the receiver raw data. Based on the receiver array configuration, its field of view is currently populated with many independent beams. However, the results of the currently adopted orbit determination process are negatively affected by the simultaneous presence of multiple grating lobes in the receiver gain pattern and by the signal quality. Within this context, this work proposes a paradigm shift in BIRALES data processing by introducing a multiple signal classification (MUSIC) approach. First, in the track estimation phase, multiple signal directions of arrival are determined, at any time instant, from the data correlation matrix. The multiplicity of the solutions is due to the array geometry and yields ambiguity in track reconstruction. For the catalogued objects, this ambiguity can be solved by exploiting the availability of their orbital estimates. For the uncatalogued ones, it is solved by clustering the candidate signal directions of arrival and identifying the correct track using slant range, Doppler shift and signal to noise ratio measurements. Although introduced for BIRALES, the applicability of the method extends to any SST survey radar with an array receiver and with the ability to correlate the signals detected by each receiver element.

Finally, algorithm performances and robustness are assessed on a large set of synthetic passes as well as on real measurements.

Keywords: Space Surveillance and Tracking, MUSIC, Adaptive beamforming, Radar array, Orbit determination

1. Introduction

Space pollution has become a major concern for space agencies and institutions all around the world, since the number of man-made objects orbiting the Earth has dramatically increased. In around 60 years of space activities, more than 6200 successful launches have taken place, to which approximately 12980 objects have been placed in Earth orbit [1]. Among these, 8290 are still orbiting, and only 5400 are active satellites. Furthermore, about 630 break-ups, explosions, collisions, or anomalous events resulting in fragmentation have been recorded, which have further contributed to the increase in the orbiting population of man-made objects.
Space debris are all artificial objects including fragments and elements thereof, in Earth orbit or re-entering the atmosphere, that are non functional [2]. Half of them is represented by entire objects (e.g. inactive satellites or launchers upper stages), while the other half is composed by fragments of various shape and size or from objects lost during previous missions (coverage, strap, etc.).The US Space Surveillance Network regularly tracks and maintain an orbital catalogue of about 30,000 space debris. However, current statistical models provide estimates on the number of orbiting objects in the order of 36500 for objects greater than 10 cm, 1000000 between 1 cm and 10 cm and 330 million between 1 mm and 1 cm.
The presence of space debris may jeopardize the operative mission of active satellites. The consequences of a possible collision between an operative satellite and a space debris ranges from cumulative erosion of satellite surface, for debris smaller than 0.1 mm, to possible catastrophic aftermaths for the satellite, with the generation of thousands of additional pieces of debris and inevitable environmental drawbacks and possible cascade effects [3].
This hazard calls for the crucial adoption of countermeasures aiming at reducing mission-related risks. Specific Space Surveillance and Tracking (SST) programs were started to build the expertise required to manage the challenges posed by the space traffic control problem. Active removal methodologies are investigated and, moreover, collision risk assessment is performed daily

by satellite operators who are provided with Conjunction Data Messages [4] to support decisions on the execution of collision avoidance manoeuvres. In addition, in-orbit fragmentations are detected and characterized, and uncontrolled re-entry predictions of objects are regularly produced to estimate on ground risks.

Collision risk assessment, fragmentations monitoring and re-entry predictions rely on the accurate estimation of the orbiting objects state, which is derived from observations performed by optical, radar and laser sensors. These sensors can measure angles (all of them), slant range (radar and laser sensors) and Doppler shift information (only radars). They can be subdivided into tracking and survey sensors: the former observe the object by tracking it, whereas the latter detect objects while they cross the sensor Field of View (FoV). At an international level, the most remarkable survey radar system is the Space Fence, which is theoretically able to perform up to 1.5 million observations per day. It has been declared to be operational by U.S. Space Force on March 28, 2020 [5].

Following the decision No. 541/2014/EU, the European Parliament and Council established the European SST (EUSST) support framework. This framework is implemented by the EUSST Consortium, subscribed in 2015, in cooperation with the European Union Satellite Centre (SatCen), and currently composed by seven member states (France, Germany, Italy, Poland, Portugal, Romania, and Spain). They grant an autonomous European capability able to safeguard the European economies, societies and citizens that rely on space-based applications such as communication, navigation and observation. EUSST services are based on a sensor network to survey and track space objects in all orbital regimes. The network currently relies on 42 sensors of the Member States of the SST Consortium (including radars, optical and laser ranging stations)[6]. Several operating ground based radar systems belong to EUSST consortium and the most remarkable ones are described hereafter.

The German Tracking and Imaging RAdar (TIRA), developed and operated at Fraunhofer FHR, combines two radars: a tracking radar operated in L-band with a center frequency of 1.3 GHz and an imaging radar operated in Ku-band with a center frequency of 16.7 GHz [7]. The French GRAVES system (Grand Réseau Adapté à la Veille Spatiale) is a bistatic surveillance radar, whose transmitter grants a total coverage of 180° in Azimuth and whose receiver exploits a digital beamforming performed in more than one thousand different directions [8] [9], and this allows the system to detect

each satellite at least once every 24 hours. The Spanish S3TSR exploits a close monostatic configuration, in which transmitting and receiving antennas are separated electronically scanning arrays [10]. The German Experimental Space Surveillance and Tracking Radar (GESTRA), developed in recent years, is a close monostatic pulsed phased array radar capable to accomplish space surveillance observations in LEO up to altitudes of 3000 km [11], [12], [13].

The Italian Bistatic Radar for Leo Survey (BIRALES) is a bistatic radar sensor which, in addition to Doppler shift and slant range measurements, is able to provide angular track, thanks to a static multibeam [14] [15]. Unfortunately, the array geometry of the BIRALES receiver introduces a spatial ambiguity which provokes the simultaneous presence of multiple grating lobes in the sensor FoV [16]. This makes the multibeam approach for track reconstruction quite sensitive to the geometry of the observations and, in specific cases, unreliable. Thus, the objective of this paper is to propose a new approach to process BIRALES data to solve the angular track reconstruction problem. More specifically, this work proposes to process the signal Covariance Matrix (CM) to derive the related Direction Of Arrival (DOA) at each time instant, and these estimations are then clustered to obtain the angular track in the receiver FoV. Since multiple solutions can appear due to the receiver array geometry, dedicated ambiguity solving criteria are also presented to select the correct solution.

Although introduced here for BIRALES, the applicability of the method extends to any SST survey radar that is provided of an arbitrary shape array as receiver station, and of a signal processing chain able to correlate the signals detected by each receiver element (to derive the covariance matrices). In addition, similarly to BIRALES, if any estimation ambiguity appears due to the array geometry, one of the presented ambiguity solving criteria can be used.

The paper is organized as follows. BIRALES sensor is introduced in Sec. 2. Then, a brief description of the orbit determination methodologies adopted in this work and the general theory of beamforming array processing are presented in Sec. 3 and Sec. 4 respectively. In particular, the track reconstruction problem is tackled by means of an adaptive beamforming technique, which estimates the signal DOA. Based on this, the new algorithm for track reconstruction is presented in Sec. 5. Finally, the performance of the proposed method is assessed on both synthetic and real data, in Sec. 6 and Sec. 7 respectively.

2. Bistatic Radar for Leo Survey

BIRALES is an Italian bistatic radar sensor of the EUSST sensor network. Its transmitter is the TRF (Trasmettitore a Radio Frequenza) located at the Italian Joint Test Range of Salto di Quirra in Sardinia, which is able to supply a maximum power of 10 kW in the bandwidth 410-415 MHz [15]. BIRALES receiver is part of the Northern Cross radio telescope of the Radio Astronomical Station of Medicina (Bologna, Italy), which consists of two perpendicular branches: the East-West (E-W) arm is 564 m long and is made of a single 35 m wide cylindrical antenna, whereas the North-South (N-S) branch is made of 64 parallel antennas each 23.5 m long and 7.5 m wide. The portion dedicated to the BIRALES receiving antenna is called "1N-section", which is an array composed of 8 cylindrical parabolic concentrators belonging to the N-S arm. Each cylinder contains four receivers installed on the focal line (aligned with the E-W direction). Therefore, the receiving system is composed of a matrix of 8x4 receivers spaced 5.67 m in E-W (d_{E-W}) and 10 m in N-S (d_{N-S}), as represented in Fig. 1.

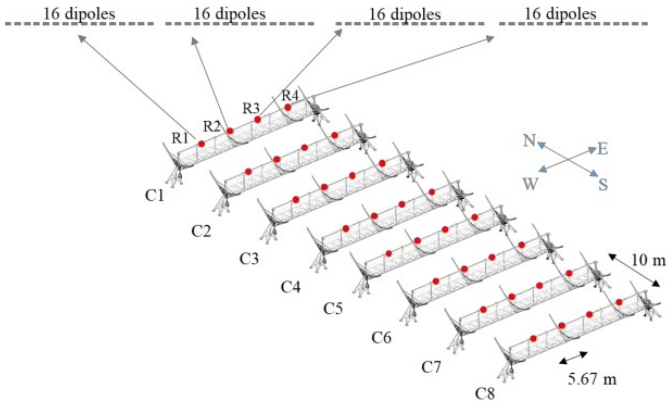


Figure 1: BIRALES receivers (red dots) installed along the antenna focal line. Each receiver contains 16 dipoles.

The 8 cylinders of the 1N-section can be mechanically pointed only in elevation (El_{RX}) along the local meridian. The mechanical elevation limits are $42° < El_{RX} < 90°$ both in North and South pointing configuration. This mechanical pointing involves all the array elements. With a total collecting area of about 1400 square meters, the system allows to detect small objects with a size of 10 cm at 2000 km slant range (SR). The FoV is $5.7° \times 6.6°$ (at

half power beam width).
BIRALES exploits two different systems, working at the same time: a multibeam Continuous Wave (CW) unmodulated radar system, operating at 410 MHz, and a single beam pulse compressed radar system, based on a pulsed chirp at 412.5 MHz with a bandwidth of 4 MHz, which is used to measure the SR [14]. Since the receiver single beam for the compressed pulse covers partially the receiving antenna FoV, slant range measurements are available only for a portion of the pass over BIRALES FoV.
The data of each detection are collected in a BIRALES Tracking Data Message (TDM) file [17], which contains, for each illuminated beam, the corresponding measured Signal to Noise Ratio (SNR) profiles, Doppler shift (DS) and SR. Thanks to dedicated calibration campaigns, the SR and DS measurements errors were assessed to be 30 m and 10 Hz respectively.
Based on its receiver array configuration, BIRALES currently exploits 32 digitally formed beams, whose direction is kept fixed in the FoV. The multibeam configuration in the receiver FoV is represented in Fig. 2, where the blue circle is the beam currently used for slant range measurement, which is obtained electronically by combining only 3 cylinders out of 8. The angles $\Delta\gamma_1$ and $\Delta\gamma_2$ represent the angular deviation from the Line of Sight (LOS). Theoretically, as soon as the observed object crosses a beam, the latter is expected to generate data. Thus, collecting all measurements along the entire pass should eventually provide the time history of the angular coordinates in the receiver FoV.
Unfortunately, the receiver array geometry introduces a spatial ambiguity. Indeed, even if, in the receiver reference frame, the mutual distances among array elements vary with the receiver elevation, they are always larger than half-wavelength (being the wavelength $\lambda = 0.73$ m) in both directions. Consequently, multiple grating lobes simultaneously appear in the sensor FoV for any beam, and their shape and mutual spacing depends on the receiver elevation. Thus, it is not straightforward to link the beam illumination to a specific direction in the receiver FoV. By collecting the contribution of the 32 beams, the overall gain pattern turns out to be relatively complex and the angular track reconstruction difficult to be achieved.
In previous works, the Multibeam Orbit Determination Algorithm (MODA) was developed to address the angular track reconstruction problem in this multibeam configuration, by exploiting both the DS and the SR measurements at the same time [16]. Despite the interesting performances on numerical simulation, when dealing with real observations, the method tends

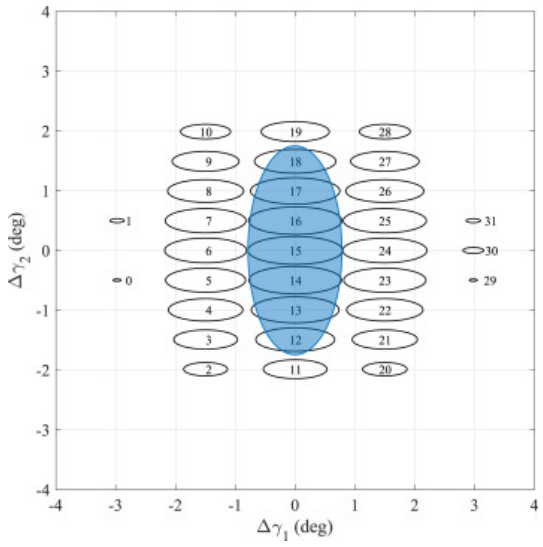


Figure 2: Multibeam configuration of BIRALES receiver. Contours define the -3 dB beamwidth of each beam main lobe with respect to the RX main lobe maximum gain. The blue ellipse represents the single analogue beam used for slant range measurements.

to be affected by the lobe ambiguity problem due to several factors, which may generate coarse angular coordinates estimation, with a maximum error of about 2.5 deg for passes with peculiar geometries. Furthermore, it is worth remarking that the angular track can only be estimated if both DS and SR measurements are available and reliable.

As mentioned in Sec. 1, the objective of this paper is to propose a reliable new method to process BIRALES data to solve the angular track reconstruction problem for both catalogued and uncatalogued resident space objects. Furthermore, the proposed method reduces the requirements on the quantities to be measured to estimate the angular profiles. More specifically, it removes the need of DS and SR measurements for catalogued objects and avoids the simultaneous need of the two measurements in the uncatalogued case.
The high-level scheme of the proposed approach (detailed in Sec. 5) is reported in Fig. 3. Given the input measurements, the process first addresses the track reconstruction problem and then solves the ambiguity caused by the receiver array geometry, by possibly exploiting additional observation data. Finally, the orbit determination is run, providing orbital mean state $\widehat{\boldsymbol{x}}$

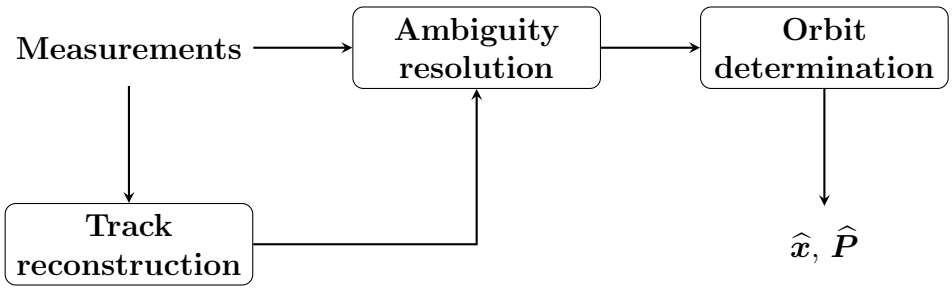


Figure 3: Proposed approach flow diagram.

and covariance $\widehat{\boldsymbol{P}}$.

3. Orbit Determination

In order to determine the orbital state of an observed object, sensor measurements can be processed in two ways, depending on whether the data, at the end of a correlation procedure, refer to a catalogued object or not.
In the catalogued case, orbital state predictions of the object are available. These predictions are refined using the measurements in a Refined Orbit Determination (ROD) process. In this context, a commonly adopted technique is the Non-Linear Least Squares approach, which iteratively modifies the orbital estimate to fit the measurements; the result is the estimated orbital mean state and its covariance, which is retrieved from the process residuals [18].
For uncatalogued objects, instead, no prediction is available and only measurements can be exploited. In this case, an Initial Orbit Determination (IOD) is performed. The Non-linear Least Squares approach could still be applied, although it may turn out to be quite unstable, mainly due to the lack of a sufficiently accurate first guess of the IOD solution. Thus, alternative methodologies have been developed by the scientific community, which are applied depending on the available measurements.
When the radar measurements include SR, the algorithm described in [19] represents a valid approach. Starting from the inertial sensor position and angular and range measurements, the method computes the object orbital position at any epoch. The related covariances can be derived from measurement uncertainty with an unscented transformation (UT) [20], by projecting the sigma points from the measurement space to the object position. Then,

the algorithm proceeds iteratively by modifying the orbital mean state with a fixed-point update process, starting from a first guess (e.g. obtained with a keplerian circular orbit assumption). Finally, the orbital state covariance is determined by transforming all individual covariances using the linear approximation. It is worth mentioning that, if an orbital prediction (retrieved, for example, from Two-Line Elements TLE [21]) is exploited as first guess, this procedure can work in a ROD process as well.
This IOD method can also be applied when SR measurements are not directly available, as they can be reconstructed from angular and DS measurements. For this purpose, the procedure proposed in [22] is applied. From DS and the transmitted frequency, the derivative $d\,\mathrm{SR}/dt$ can be computed and used to reconstruct SR profile at any epoch, considering a guessed initial value SR_0:

$$\mathrm{SR}\,(t) = \mathrm{SR}_0 + \int_{t_0}^{t} \frac{d\,\mathrm{SR}}{dt}\, dt \tag{1}$$

Based on this operation and from angular measurements, inertial positions of the observed object can be computed, the Lambert's problem solved and the specific orbital energy of the connecting arc estimated, for any epoch. Overall, the process searches for the value SR_0 which minimizes the specific energy standard deviation.
Fig. 4 represents the proposed application of this approach, which first performs the minimization on a coarse grid, by using a golden section search and parabolic interpolation. The resulting SR_0 is the first guess entering a Non-linear Least Squares process, that refines the estimate by iteratively performing IOD. The final estimate SR_0 is used to derive the SR profile at all the observation epochs, according to Eq. 1. Finally, orbital mean state and covariance are computed according to the radar IOD procedure.

4. Track reconstruction problem

As described in Sec. 2, this work aims at replacing the static multibeam used in MODA algorithm with a new approach. Adaptive beamforming techniques are here discussed, which estimate the DOA of the impinging signals by properly fusing data collected by the sensor array, where their relative separation provides a sample of the wavefront in the spatial domain. In this framework, the current section deals with the track reconstruction problem.

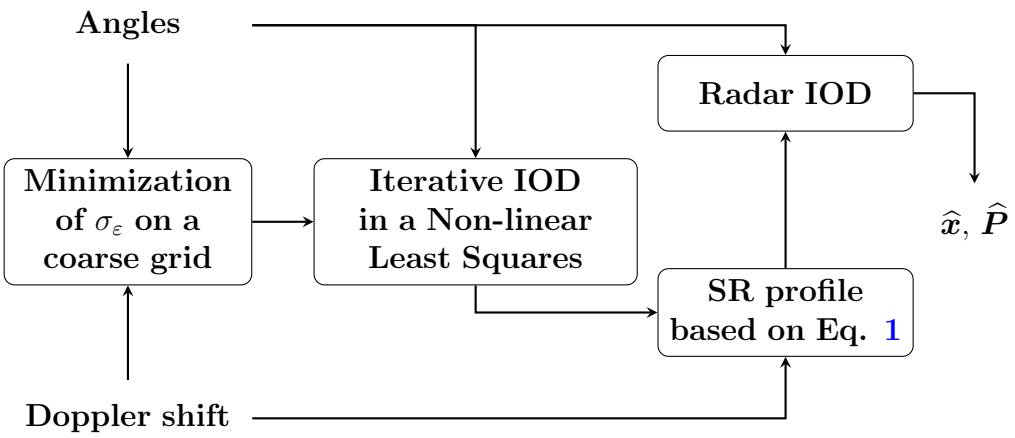


Figure 4: Flow diagram of the radar IOD procedure if angles and Doppler shift are present.

4.1. Data model

Consider the case of a source impinging on a planar rectangular sensor array consisting of $M = N_x \times N_y$ uniformly distributed elements and with physical spacing d_x and d_y. The signal emitted is assumed to be a narrow-band complex electro-magnetic wave, so that a time delay corresponds to a phase shift.
Let $\Delta\gamma_1$ and $\Delta\gamma_2$ denote the two angular deviations relative to the LOS (in Azimuth and Elevation respectively). From [23], the direction cosines corresponding to the DOA are:

$$\begin{aligned} u &= \sin\Delta\gamma_1 \cos\Delta\gamma_2 \\ v &= \sin\Delta\gamma_2 \end{aligned} \tag{2}$$

The planar wave on a generic position $\boldsymbol{r}$ can be written as $E(t) = Ae^{j(\omega t - k\boldsymbol{r}\cdot\boldsymbol{u})}$ where $k = 2\pi/\lambda$ is the wave number and $\boldsymbol{u}$ is the unit vector of the impinging DOA.
From [24], the distances measured in wavelength are:

$$\begin{aligned} d_{x_\lambda} &= \frac{d_x}{\lambda} \\ d_{y_\lambda} &= \frac{d_y}{\lambda} \end{aligned} \tag{3}$$

After having defined the electric angles as:

$$\begin{aligned} \phi_x &= 2\pi d_{x_\lambda} u \\ \phi_y &= 2\pi d_{y_\lambda} v \end{aligned} \tag{4}$$

it is possible to write the steering vector corresponding to the m-th line of sensors (where $m = 0 : N_y - 1$) as

$$\boldsymbol{a}_m(\boldsymbol{\Delta\gamma}) = \begin{bmatrix} e^{-jm\phi_y} \\ e^{-j(\phi_x + m\phi_y)} \\ \vdots \\ e^{-j((N_x-1)\phi_x + m\phi_y)} \end{bmatrix} \tag{5}$$

where the bold notation $\boldsymbol{a}_m(\boldsymbol{\Delta\gamma})$ indicates that the steering vector indirectly depends on the vectorial parameter $\boldsymbol{\Delta\gamma} = [\Delta\gamma_1\,,\,\Delta\gamma_2]^T$. By stacking the steering vectors corresponding to the lines of the array, it is possible to define the $M \times 1$ steering vector ($M = N_x \times N_y$) as

$$\boldsymbol{a}(\boldsymbol{\Delta\gamma}) = \begin{bmatrix} \boldsymbol{a}_0(\boldsymbol{\Delta\gamma}) \\ \vdots \\ \boldsymbol{a}_{N_y-1}(\boldsymbol{\Delta\gamma}) \end{bmatrix} \tag{6}$$

Then, the signal received by the array at any time instant can be expressed as:

$$\boldsymbol{x}(t) = \boldsymbol{a}(\boldsymbol{\Delta\gamma})s(t) + \boldsymbol{n} \tag{7}$$

where $s(t)$ is the envelope of the signal emitted by the source and impinging on the array, and $\boldsymbol{n}$ is the process noise.
Based on $\boldsymbol{x}(t)$, the CM can be computed as:

$$\boldsymbol{R_{xx}} = E\left[\boldsymbol{x}(t)\boldsymbol{x}(t)^H\right] \tag{8}$$

where $E\left[...\right]$ is the expected value operator and $\boldsymbol{x}(t)^H$ is the hermitian of $\boldsymbol{x}(t)$.
In the discrete time domain, considering N_k as the number of snapshots referred to the same signal sampling, $s(t)$ can be expressed as $\widehat{\boldsymbol{s}}$ (a vector of N_k elements) and Eq. 7 becomes:

$$\widehat{\boldsymbol{x}} = \boldsymbol{a}(\boldsymbol{\Delta\gamma})\widehat{\boldsymbol{s}} + \widehat{\boldsymbol{n}} \tag{9}$$

where $\widehat{\boldsymbol{n}}$ is the discrete time domain noise affecting the signal. In this way, the discrete CM referred to a signal sampling can be expressed as:

$$\widehat{\boldsymbol{R}}_{\boldsymbol{xx}} = \frac{1}{N_k} \sum_{k=1}^{N_k} \boldsymbol{x}_k \boldsymbol{x}_k^H \tag{10}$$

Considering BIRALES receiver array, $M = N_x \times N_y = 32$, being $N_x = 4$ (R1, R2, R3 and R4 in Fig. 1) and $N_y = 8$ (C1, C2, .., C8 in Fig. 1). Thus, $\boldsymbol{a}(\boldsymbol{\Delta\gamma})$ dimension is 32×1 and $\widehat{\boldsymbol{R}}_{\boldsymbol{xx}}$ size is 32×32 regardless the snapshot number N_k.

4.2. MUltiple SIgnal Classification

Various estimation algorithms can be used to compute the DOA. The adaptive beamforming techniques can be categorized in three families [24]: the approaches that linearly combine sensor outputs (such as Minimum Variance Distortionless Response, MVDR), the ones that consider problem statistics (such as Stochastic Maximum Likelihood estimation, SML) and the approaches that apply spectral decomposition of the signal CM. This work deals with the third family and focuses on the MUltiple SIgnal Classification (MUSIC) algorithm [25].

Ideally, without any noise contribution, $\boldsymbol{R}_{\boldsymbol{xx}}$ rank is equal to the signal sources number N_s. In real scenarios instead, which are affected by noise, $\boldsymbol{R}_{\boldsymbol{xx}}$ shows N_s eigenvalues much larger than the other $M - N_s$. Therefore, it is possible to split $\boldsymbol{R}_{\boldsymbol{xx}}$ space in signal and noise subspaces, which are assumed to be orthogonal (based on the assumption that signal and noise are uncorrelated). Denoting the largest eigenvalues matrix as $\boldsymbol{\Lambda_s}$ and the corresponding eigenvectors subspace as $\boldsymbol{U_s}$ and, similarly, indicating noise subspace matrices as $\boldsymbol{\Lambda_n}$ and $\boldsymbol{U_n}$, the CM can be decomposed as:

$$\boldsymbol{R}_{\boldsymbol{xx}} = \boldsymbol{U_s} \boldsymbol{\Lambda_s} \boldsymbol{U_s}^H + \boldsymbol{U_n} \boldsymbol{\Lambda_n} \boldsymbol{U_n}^H \tag{11}$$

MUSIC method assumes that $\boldsymbol{U_s}$ and $\boldsymbol{U_n}$ span orthogonal complements and it can be proved that $\boldsymbol{U_s} \boldsymbol{\Lambda_s} \boldsymbol{U_s}^H$ has $M - N_s$ eigenvalues equal to zero.

The estimate $\boldsymbol{\Delta\gamma}$ can thus be computed through the maximization of the following spectrum, which represents the array response to the impinging wave:

$$P(\boldsymbol{\Delta\gamma}) = \boldsymbol{a}(\boldsymbol{\Delta\gamma})^H \boldsymbol{U_s} \boldsymbol{U_s}^H \boldsymbol{a}(\boldsymbol{\Delta\gamma}) \tag{12}$$

An alternative formulation is obtained by considering that $\boldsymbol{U_n}^H \boldsymbol{a}(\boldsymbol{\Delta\gamma}) = 0$. Due to the orthogonality between signal and noise subspaces, the estimate

$\boldsymbol{\Delta\gamma}$ can be computed in an alternative way through the maximization of the following spectrum:

$$P(\boldsymbol{\Delta\gamma}) = \frac{1}{\boldsymbol{a}(\boldsymbol{\Delta\gamma})^H \boldsymbol{U_n} \boldsymbol{U_n}^H \boldsymbol{a}(\boldsymbol{\Delta\gamma})} \tag{13}$$

Or by considering that $\boldsymbol{U_n}\boldsymbol{U_n}^H = \boldsymbol{I} - \boldsymbol{U_s}\boldsymbol{U_s}^H$ (where $\boldsymbol{I}$ is a $M \times M$ identity matrix), through:

$$P(\boldsymbol{\Delta\gamma}) = \frac{1}{\boldsymbol{a}(\boldsymbol{\Delta\gamma})^H \left[\boldsymbol{I} - \boldsymbol{U_s}\boldsymbol{U_s}^H\right] \boldsymbol{a}(\boldsymbol{\Delta\gamma})} \tag{14}$$

Finally, the sensor directional properties can be taken into account by introducing a tapering action $\Upsilon_s(\boldsymbol{\Delta\gamma})$ on the total array response:

$$\Gamma(\boldsymbol{\Delta\gamma}) = P(\boldsymbol{\Delta\gamma})\, \Upsilon_s(\boldsymbol{\Delta\gamma}) \tag{15}$$

This work addresses the case of a single source observed, that is $N_s = 1$.

4.3. BIRALES pattern ambiguity

A fundamental condition must be met to have a unique solution of Eq. 14, that is:

$$\begin{aligned} \frac{d_x}{\lambda} &\leq \frac{1}{2} \\ \frac{d_y}{\lambda} &\leq \frac{1}{2} \end{aligned} \tag{16}$$

Eq. 16 is analogous in space-domain of the Shannon theorem: the spacing between samples of the signal, which is provided by the array elements position, must be lower than the half-distance between the sinusoidal peaks, that is the half-wavelength. As a consequence, if the spacing is longer than half-wavelength, spatial ambiguity (aliasing) occurs and so grating lobes appear. The shift of the i-th (in direction E-W) and j-th (in direction N-S) grating lobe with respect to the boresight, expressed in direction cosines space (Eq. 2) is [24]:

$$\begin{aligned} u &= \frac{i}{d_{x_\lambda}} \\ v &= \frac{j}{d_{y_\lambda}} \end{aligned} \tag{17}$$

where d_{x_λ} and d_{y_λ} are defined in Eq. 3.
According to Eq. 2, it is possible to express such a shift in angular coordinates as:

$$\Delta\theta_x \approx \arcsin \frac{i}{d_{x_\lambda}}$$
$$\Delta\theta_y = \arcsin \frac{j}{d_{y_\lambda}} \tag{18}$$

which holds as long as $\Delta\theta_y$ (that is the angular shift, in direction N-S, of the j-th grating lobe with respect to the boresight) is small, which allows the approximation $\cos\Delta\theta_y \approx 1$.
As mentioned in Sec. 2 about the multibeam configuration, BIRALES receiver does not fulfil the requirement expressed in Eq. 16, being $\lambda = 0.73$ m, $d_x = 5.67$ m and $d_y = 10$ m . This generates an ambiguity in the array response to the impinging signal and multiple peaks (that is, multiple solutions) are simultaneously present at any epoch, as represented in Fig. 5, which shows MUSIC output. The mutual angular distance among these

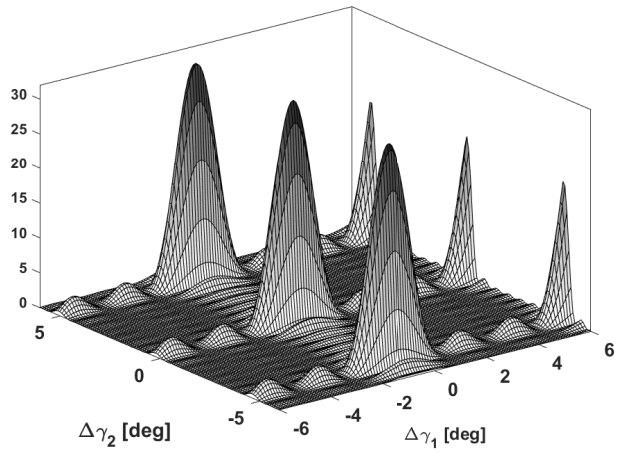


Figure 5: BIRALES 3D array response based on MUSIC.

peaks is defined according to Eq. 18.
In order to overcome this problem, additional information on the observed object shall be exploited. To this aim, the orbit determination methodologies introduced in Sec. 3 are applied in Sec. 5 to establish reliable ambiguity solving criteria.

5. Music Approach for Track Estimate and Refinement

Ad-hoc solutions shall be identified for the DOA estimation ambiguities which are introduced by the BIRALES array configuration, by possibly exploiting problem geometry and pass predictions. In this framework, the Music Approach for Track Estimate and Refinement (MATER) algorithm has been developed, to successfully process BIRALES measurements to estimate the signal DOA by solving the ambiguities and performing OD. As the name suggests, the algorithm core is composed of two steps: track estimate, performed with MUSIC, and track refinement, where clustering, regression and ambiguity solving criteria are adopted.

5.1. Catalogued objects

In case the observed object is catalogued (i.e., when BIRALES is used to track objects provided with catalogued orbital estimates), MATER processes BIRALES measurements as illustrated in Fig. 6. In the track estimate phase, the DOA is estimated from the CM eigen-decomposition, thanks to an optimization process aimed at maximizing Eq. 15. The reference track (derived from pass prediction) can directly be used as first guess in the optimization, such that the DOA corresponding to the closest peak is selected. In this way, if the first guess is sufficiently close to the actual DOA (i.e., if the a priori orbital estimate is sufficiently accurate), the DOA ambiguity is solved and a single track is obtained, as reported in Fig. 7 for a generic LEO pass.

Once the DOA estimate at each observation epoch has been computed, the algorithm proceeds to the track refinement phase, whose purpose is to derive the time evolution of the object angular coordinates in the sensor reference frame during the pass. This goal is achieved by performing a quadratic regression in time on the two angular coordinates separately, such that the time-dependent profiles $\Delta\gamma_1(t)$ and $\Delta\gamma_2(t)$ are obtained. The result is shown in Fig. 8, which shows the track obtained (based on synthetic data) for a generic pass.

Then, the reconstructed track enters a ROD process based on the procedure described in Sec. 3. Thus, an index assessing the correlation between the estimated orbital state and measurements is computed. If such a correlation index satisfies the threshold, the OD process is considered successful, otherwise, a radar IOD process is run (with the SR measured or derived from

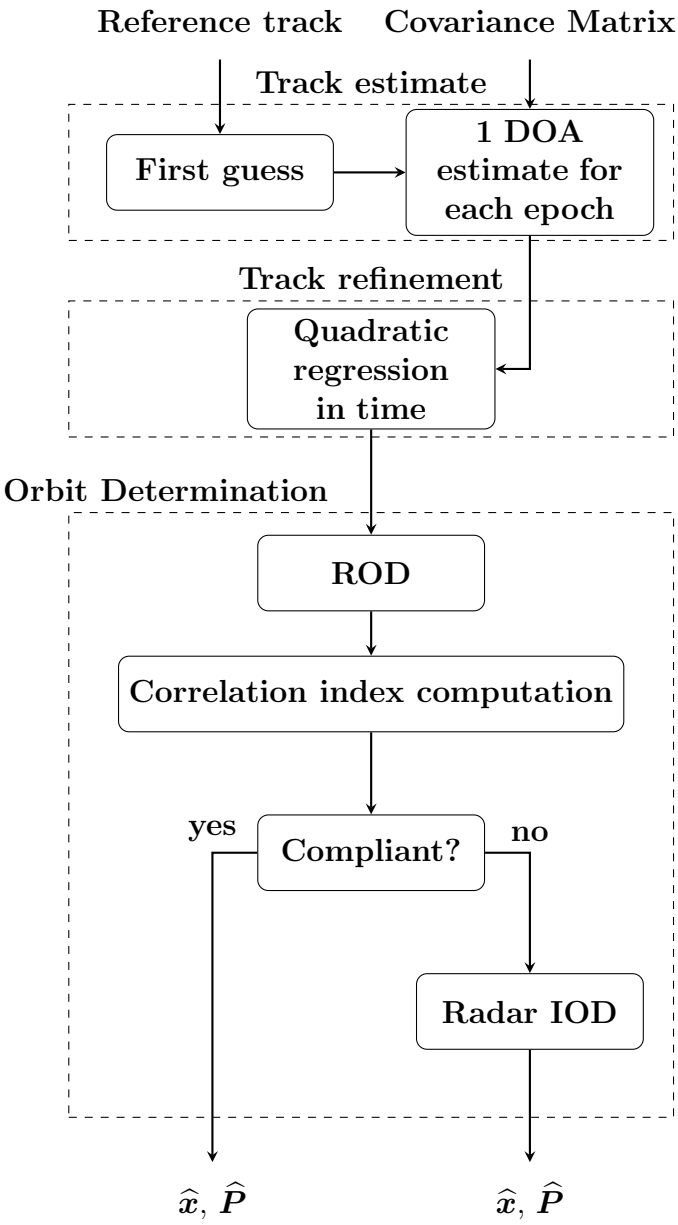


Figure 6: MATER: catalogued case flowchart.

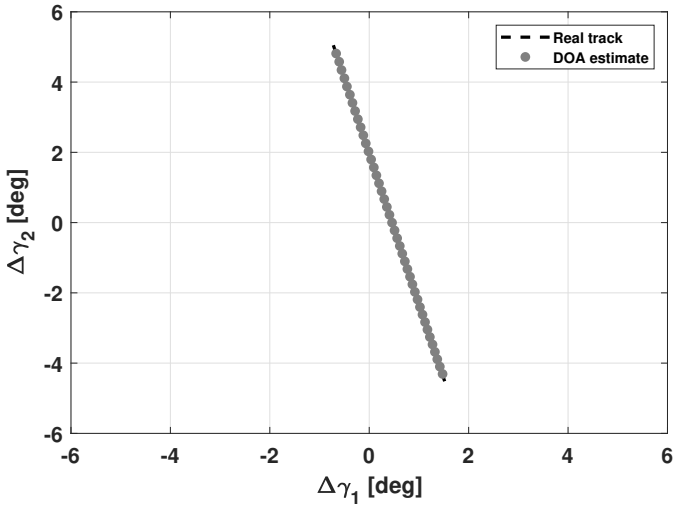


Figure 7: Catalogued case: track estimate result.

DS). The final outputs are the orbital mean state $\widehat{\boldsymbol{x}}$, and its covariance $\widehat{\boldsymbol{P}}$.

5.2. Uncatalogued objects with either SR or DS measurements

For uncatalogued objects (i.e., when the detected measurements do not correlate to any catalogued object) the process adopted by MATER is schematized in Fig. 9. The CM is the only input, as no pass prediction is available, and the track estimate phase starts by performing a coarse computation on a grid of angular coordinates, aimed at identifying the highest N_p peaks of the pattern obtained from Eq. 14. The peaks searching is performed by identifying the global maximum first. Then, the other $N_p - 1$ peaks coordinates are determined analytically, according to the angular shift of Eq. 18. These N_p angular coordinates pairs represent the first guess for the maximization process of Eq. 15. Thus, N_p angular positions in the receiver FoV are identified at each epoch. As a consequence, multiple candidate tracks appear in the sensor FoV, among which only one is correct (see Fig. 10).
In order to identify these multiple candidates, the track refinement phase starts by clustering the DOAs according to a RANdom SAmple Consensus (RANSAC) process, which iteratively performs a regression among a data subset, distinguishing inliers from outliers. In this phase, clusters that do not satisfy a population threshold are discarded. At the end, a quadratic

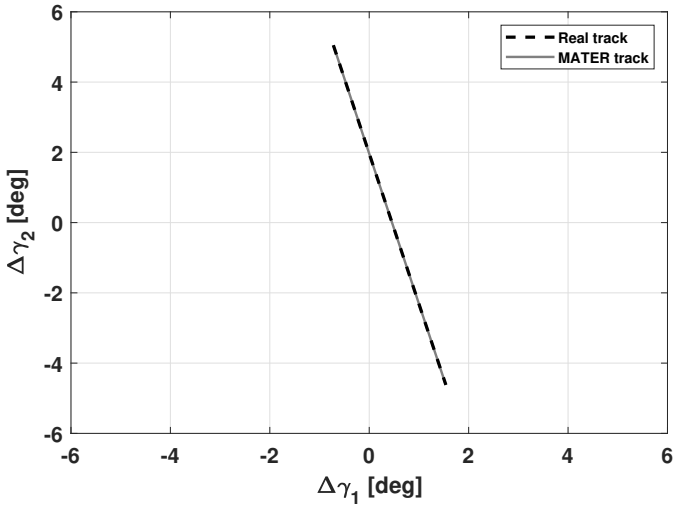


Figure 8: Catalogued case: track refinement result.

regression in time is performed on the two angular coordinates for each cluster, such that time-dependent profiles $\Delta\gamma_1(t)$ and $\Delta\gamma_2(t)$ are obtained for all candidates, as represented in Fig. 11. It can be noticed that some side points present in Fig. 10 do not have any related track, since they form clusters which do not satisfy the population threshold and they have been rejected.
At this point, multiple track candidates are present and the unfeasible solutions can be rejected first. Enlarging BIRALES 3 dB FoV (described in Sec. 2) to $[-6°, +6°]$ (such that all significant signal contributions are kept), the correct track is not expected to spend significant time out of that region, as it is unlikely that the receiver array detects signal while the source is out of the FoV. Therefore, a threshold on the maximum percentage of time spent out of the FoV shall be respected (5% in this work). The result is shown in Fig. 12, where it can be observed that some track candidates have been rejected.
After the above filtering action, multiple candidates may still appear (like in Fig. 12) and proper criteria must be applied to select the correct solution. Four procedures have been investigated to this purpose, which are applied depending on the available measurements. The first three, which exploit additional measurements, are described as follows, while a separate paragraph is afterwards dedicated to the fourth one.

The first one is the SR criterion: the correct track is the one which,

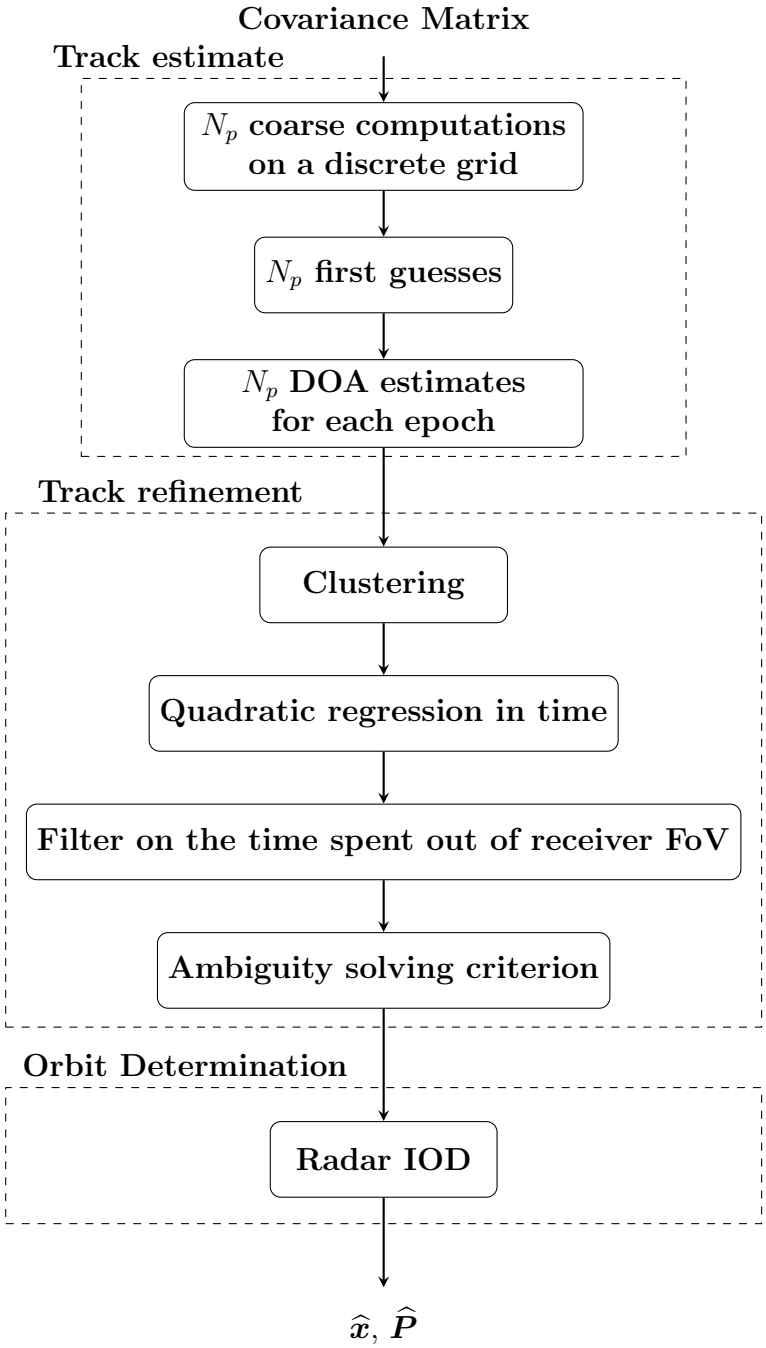


Figure 9: MATER: uncatalogued case process flowchart.

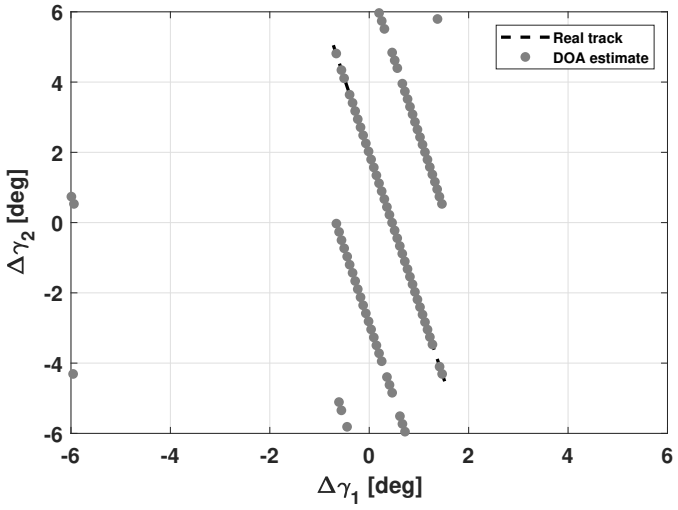


Figure 10: Uncatalogued case: track estimate result.

combined with DS and according to the procedure described in Sec. 3, returns the predicted SR profile that best matches the measured one. This criterion provides a straightforward process to solve the ambiguity, although it needs both SR and DS measurements.

The second procedure is the SNR criterion, according to which the correct track is the one whose predicted SNR profile best matches the measured one. The predicted SNR is derived from [20]:

$$SNR = 10\ \log_{10}\left(\frac{P_{rx}}{k\,Bw\,T_{eq}}\right) \tag{19}$$

where $k = 1.380658e-23$ is the Boltzmann's constant, Bw is the channel bandwidth and T_{eq} is the equivalent temperature of the system. For a bistatic radar, the received power P_{rx} is defined as:

$$P_{rx} = \frac{P_{tx}\,G_{tx}\,G_{rx}\,RCS\,c^2}{(4\pi)^3\ f_c^2\,\rho_{TX}^2\,\rho_{RX}^2} \tag{20}$$

where P_{tx} is the transmitted power, G_{tx} and G_{rx} are transmitter and receiver gain respectively, RCS is the object radar cross section, c is the light speed, f_c is the transmitted frequency, ρ_{TX} and ρ_{RX} are the distances between the orbiting object, and the transmitter and receiver respectively (so their sum is the SR).

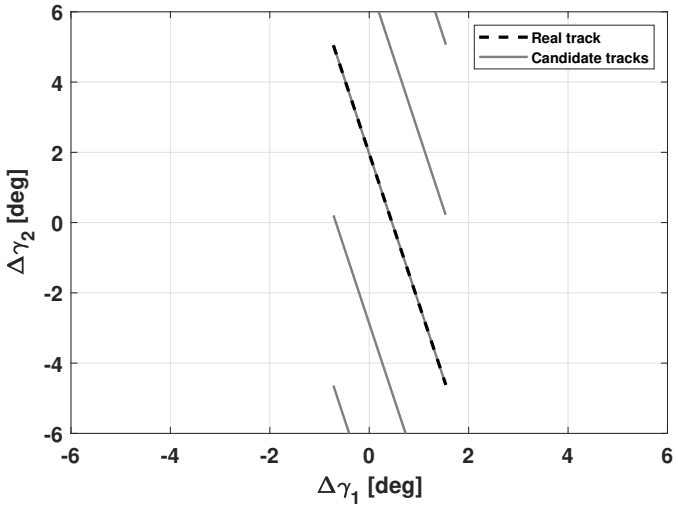


Figure 11: Uncatalogued case: candidates in the track refinement phase.

Since the contributions G_{rx}, G_{tx}, ρ_{TX} and ρ_{RX} depend on the relative position between the observed object and the ground stations, the predicted SNR profiles computed from the candidate tracks are expected to significantly differ one from another and this makes the SNR criterion theoretically robust. Furthermore, this criterion solves the track ambiguity when only SR or DS measurements are available. In the latter case, indeed, the terms ρ_{TX} and ρ_{RX} can be derived from DS, observation epochs and track angles, according to the procedure described in Sec. 3. In order to apply this criterion, an RCS value must be assumed and it possibly introduces a bias term in the difference between the measured SNR and the predicted one. However, this term affects all candidates equally and it does not have an impact on the validity of the criterion.

The third procedure is the OD-based criterion, according to which the correct track is the one generating the orbit featuring the best correlation to the measurements. In order to determine the orbit, the radar IOD procedure described in Sec. 3 turns out to be a robust approach and the OD criterion can be applied even if only SR or DS measurements are available. Hence, any track candidate enters an IOD process: an orbital state estimate is obtained and the associated correlation index is computed, as later defined in Sec. 6. Finally the best candidate is selected.

Regardless the approach adopted, once the correct track has been se-

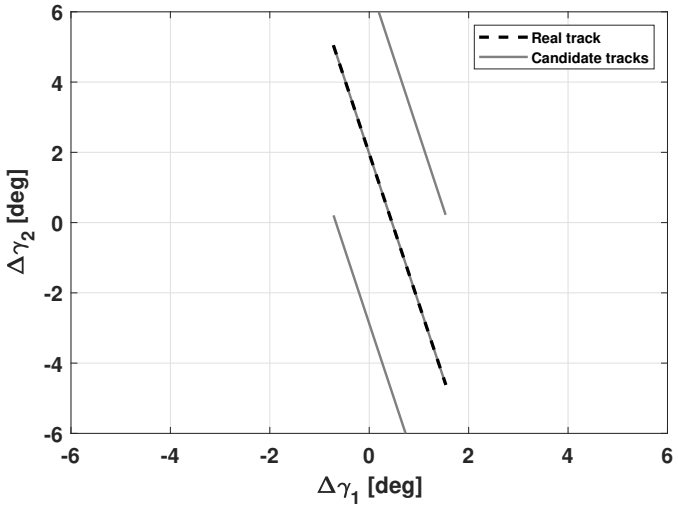


Figure 12: Uncatalogued case: feasible candidates in the track refinement phase.

lected, the OD process is run to estimate the orbital mean state $\widehat{\boldsymbol{x}}$ and its covariance $\widehat{\boldsymbol{P}}$. It is important to point out that, for the SNR and OD solving criteria, the OD phase is already contained in the track refinement.

5.3. Uncatalogued objects without SR and DS measurements

A separate process must be planned if, in the uncatalogued case, neither DS nor SR measurements are available and just the angular path can be used to solve the ambiguity. In this case, the most populated cluster criterion is applied, according to the assumption that the correct track is the one spending the longest time in the sensor FoV. This procedure affects both the track estimate and the track refinement phases and the related flowchart is presented in Fig. 13.

Based on the above assumption, in the track estimate phase a weighting action is applied to favor the central peaks. More specifically, the MUSIC pattern, reported for a generic instant in Fig. 5, is superimposed to the array element pattern, according to Eq. 15. Then, during the coarse grid computation, only the angular coordinates corresponding to the maximum peak are selected and are used as first guesses in the selection process. In this way, multiple track candidates are expected to appear at the end of the track estimation phase, as represented in Fig. 14. It is possible to observe that, when the source is in a border region of the receiver FoV, the algorithm converge to a more central ambiguous solution, like in Fig. 15.

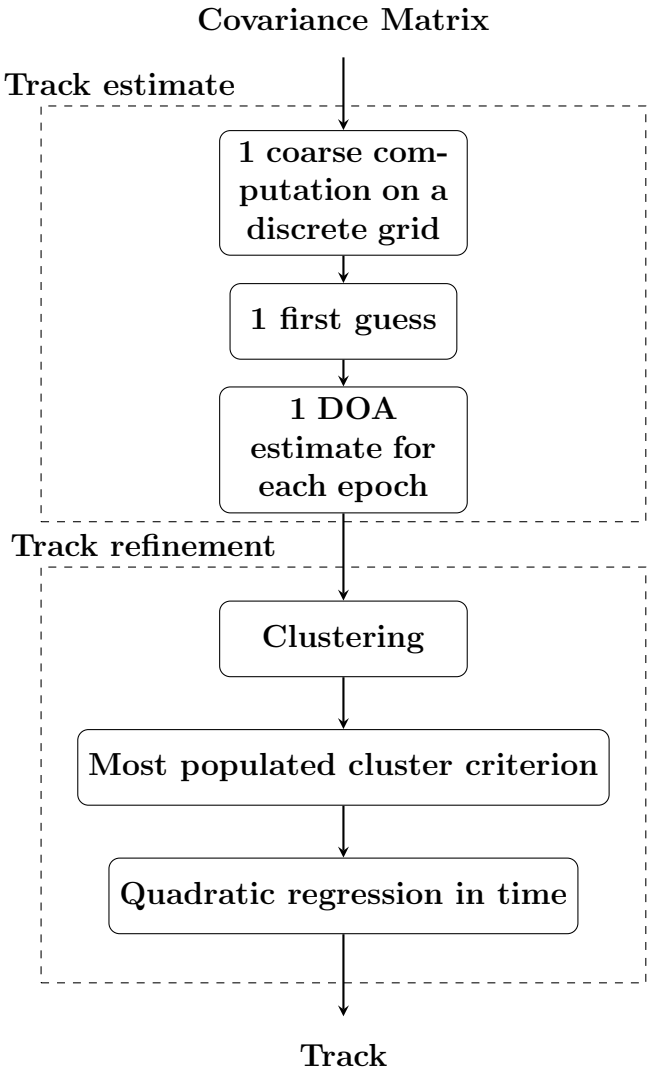


Figure 13: Uncatalogued case flowchart when neither SR nor DS are available.

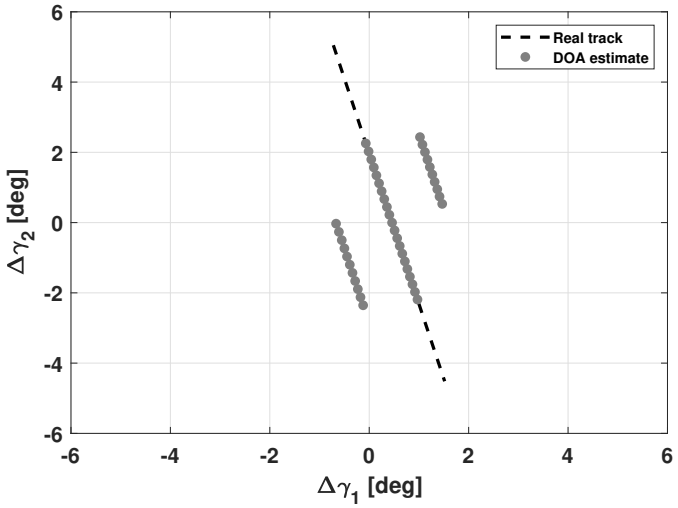


Figure 14: Uncatalogued case when neither SR nor DS are available: track estimate result.

Next, in the track refinement phase, the RANSAC clustering is performed and, according to the assumption above, the most populated cluster is selected as the one related to the correct track. Then, the quadratic regression in time is performed on the two angular coordinates to obtain $\Delta\gamma_1(t)$ and $\Delta\gamma_2(t)$. The track does not enter a radar IOD process and the angular profile of Fig. 16 is the output of the procedure.
This approach assumes that the source spends most of the pass in the central part of the sensor FoV. Consequently, it can hardly solve ambiguities for objects crossing the FoV close to the border, as it favors central solutions.

6. Numerical tests and results

The performance of MATER is assessed with numerical tests, including nominal conditions as well as a sensitivity analysis to relevant parameters.

6.1. Nominal performances

A synthetic data set (taken from [16]) composed of 899 passes related to 537 LEO objects from the NORAD catalogue is analyzed. The analysis considers an observation window of one week, from December 15 to December 21, 2018. The passes projections in the measurements space provide their nominal angular tracks, SR and DS measurements. The transmitter and receiver pointing angles, provided in terms of Azimuth and Elevation are set

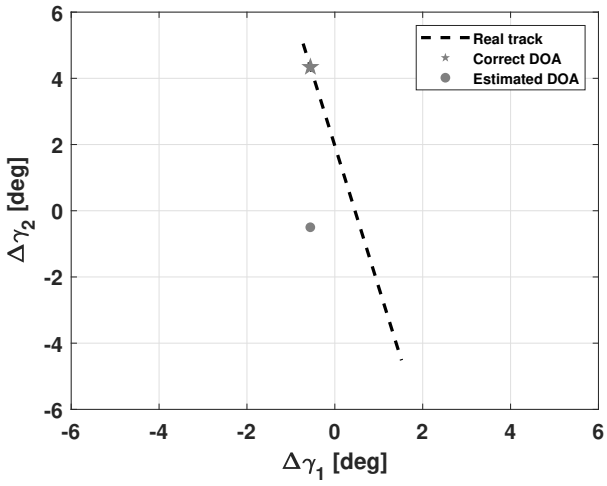


Figure 15: Uncatalogued case when neither SR nor DS are available: DOA estimation error.

to [7.69°, 40.45°] and [0°, 60°] respectively. According to [16], this configuration allows the observations to cover most objects and the angular tracks to spread over the entire receiver FoV.
Then, the data for the testing procedure are generated as follows:

- The measured SNR is simulated according to Eq. 20, with an RCS of 1 m^2 and the addition of Gaussian noise (standard deviation of 0.5 dB) to include the effect of the RCS fluctuation. Furthermore, a receiver channel bandwidth of 9 Hz is considered (which is the same as the one of the final channel of the current BIRALES multibeam configuration), together with an equivalent temperature of 86 K.

- The measured SR and DS, derived from the synthetic dataset, are artificially corrupted with a Gaussian noise coherent with the sensor accuracy described in Sec. 2.

Next, the CM is generated for each time instant along the pass, through the implementation of the formulas reported in Sec. 4, assuming an instantaneous integration of Eq. 10 with $N_k = 100$ snapshots. The signal $s(t)$ is modeled as proportional to the SNR, while the noise $n(t)$ through a Gaussian distribution, with standard deviation equal to 1.
Starting from these data, MATER is run and the resulting performances are

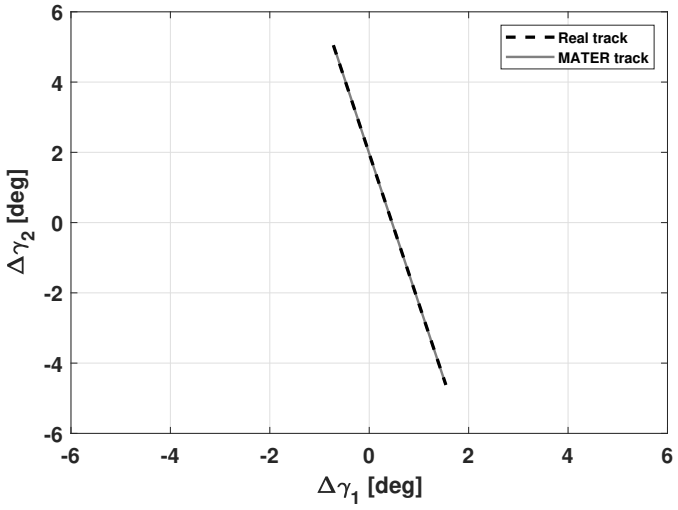


Figure 16: Uncatalogued case when neither SR nor DS are available: track refinement result.

assessed in terms of convergence rate and mean value of the root mean square errors (RMSE), computed as:

$$\eta = \sqrt{\frac{1}{N} \sum \left(\Delta\gamma - \overline{\Delta\gamma}\right)^2} \tag{21}$$

where $\overline{\Delta\gamma}$ stands for the correct angular position and N is the number of the derived angular data. The quantity η is computed only on the cases where MATER successfully converged to the solution.
Then, the correlation index $\bar{\zeta}$ between determined state and measurements is computed using the concept of Mahalanobis distance. This index is defined as the mean value of:

$$\zeta(t_i) = \left[\tilde{\boldsymbol{y}}(t_i) - \boldsymbol{y_{obs}}(t_i)\right]^T \boldsymbol{P}_{\boldsymbol{obs}}^{-1} \left[\tilde{\boldsymbol{y}}(t_i) - \boldsymbol{y_{obs}}(t_i)\right] \tag{22}$$

where $\boldsymbol{P_{obs}}$ is the constant sensor covariance (defined according to sensor accuracy), and $\boldsymbol{y_{obs}}(t_i)$ and $\tilde{\boldsymbol{y}}(t_i)$ indicate, at any epoch, the real and the synthetic measurements set, respectively. The latter are obtained from the determined state through UT [20] (accounting also for the uncertainty resulting from the orbit determination).
First of all, MATER is run by assuming that all objects are catalogued, i.e. an a priori estimate of their orbit is available. The results are summarized

in Tab. 1, which reports the success rate (in percentage), $\eta_{\Delta\gamma_1}$ and $\eta_{\Delta\gamma_2}$ (in degree) and $\overline{\zeta}$. The algorithm was able to converge in all cases. In addition, the very low values of angular error and correlation index confirm the accurate performances of MATER on the observation of catalogued objects. In addition, it is worth observing that the angular RMSE is a bit lower in the N-S direction ($\eta_{\Delta\gamma_2}$) than in the E-W direction ($\eta_{\Delta\gamma_1}$). This result can be linked to the larger number of array elements in the N-S direction, which grants higher resolution.

Success [%]	$\eta_{\Delta\gamma_1}$ [deg]	$\eta_{\Delta\gamma_2}$ [deg]	$\overline{\zeta}$
100	5.3e-04	4.2e-04	6.7e-02

Table 1: Catalogued case: statistical analysis on synthetic data.

Then, MATER is applied on the same passes in uncatalogued mode, i.e. by assuming that no a priori orbital estimates of the objects are available. The results are reported in Tab. 2. Each row in the table provides the performance obtained by one of the different solving criteria introduced in Sec. 5. For both the SNR and the OD criterion, the brackets in the first column specify which measurement is available to solve the ambiguity.

Criterion	Success [%]	$\eta_{\Delta\gamma_1}$ [deg]	$\eta_{\Delta\gamma_2}$ [deg]	$\overline{\zeta}$
SR	99.7	5.2e-04	4.3-04	1.2e-01
SNR (SR)	100	5.2e-04	4.2e-04	6.8e-02
SNR (DS)	100	5.2e-04	4.3e-04	9.1e-02
OD (SR)	100	5.1e-04	4.2e-04	6.8e-02
OD (DS)	99.9	5.1e-04	4.2e-04	6.4e-02
Most Pop.	98.1	1.0e-03	9.0e-04	6.7e-02

Table 2: Uncatalogued case: statistical analysis on synthetic data. Each row is related to one of the different solving criteria introduced in Sec. 5: SR stands for SR criterion, SNR (SR) and SNR (DS) for the SNR criterion when SR is available and when DS is available respectively, OD (SR) and OD (DS) for the OD-based criterion when SR is available and when DS is available respectively, Most Pop. for the most populated cluster criterion.

Focusing on the success rate, it is possible to note that, if the SR measurement is available and used, the SNR and the OD criteria always converge to the correct solution. On the other hand, the simple SR criterion and the OD

one with DS measurements shows some failures (in the number of 3 and 1, respectively). These failures regard passes in which more solutions are compliant with the other measurements and, consequently, the random noise associated to SR and DS profile affects the ambiguity solving process. More specifically and for example, in the SR criterion, the noisy DS profile affects the SR reconstruction process (see Sec. 3): multiple SR profiles tend to match the measured one and a wrong solution may happen to provide the best matching. In a similar way, the OD criterion with DS measurements can have multiple solutions featuring similar correlation indexes and, due to the DS noise, the wrong solution may feature a better correlation index. This problem is solved in the OD criterion with SR measurements, as no SR reconstruction from DS is performed, and in the SNR criterion, since the entire geometry of the pass is exploited and the effect of the noise is reduced. Finally, the most populated cluster criterion turns out to be an interesting option when the SR and DS measurements are not available or not reliable, since it fails only in 17 passes, all of them spending significant time in FoV side regions. A failure case of the most populated cluster criterion is represented in Fig. 17.

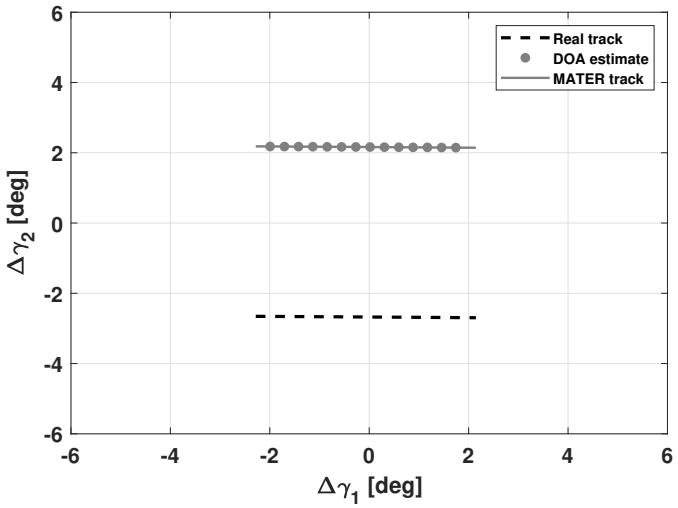


Figure 17: Uncatalogued case: erroneous track result in most populated cluster criterion, due to DOAs erroneously estimation. The algorithm converges to a more central ambiguous solution.

Overall, like in the catalogued case, the angular RMSE is a bit lower in the N-S direction ($\eta_{\Delta\gamma_2}$) than in the E-W one ($\eta_{\Delta\gamma_1}$), which is due to the higher

resolution in the former direction. Another general consideration is that the mean correlation index $\overline{\zeta}$ is comparable to the one of the catalogued case.

To sum up, based on the statistical analysis performed with the numerical tests, the track reconstruction problem can be solved for both catalogued and uncatalogued objects. In the latter case, the SNR criterion turns out to be the most reliable one, together with the OD criterion with SR measurements (which does not need the SNR profile). The SR criterion and the OD criterion with DS measurements provide a good success rate, although they featured some failures. In the case neither SR nor DS measurements are available, the track ambiguity can be solved with the most populated cluster criterion. However, this method tends to fail for passes close to the FoV border.

6.2. Sensitivity analysis

A sensitivity analysis of MATER performance is carried out in this section. In particular, the analysis aims at testing algorithm robustness, both in terms of track estimate and track refinement phase, especially in the solution of the track ambiguity problem. The uncatalogued case is investigated, as it allows to carry out an analysis more complete than the catalogued one. To solve the ambiguity, the SNR criterion with SR measurements is exploited, as it represents an optimal way to select the proper track (according to the numerical analysis shown in Sec. 6.1).

The same dataset of 899 simulated passes is generally used hereafter and the off-nominal scenarios in which the sensitivity analysis is performed are subdivided in two classes.

The first class includes scenarios that affect the algorithm performance at any level, regardless the ambiguity solving criterion adopted:

- *Different TX and RX pointing directions*: this is modeled by simulating observations in which BIRALES receiver points towards 45N (Azimuth 0° and Elevation 45°) and 90 (Elevation 90°). Indeed, it is fundamental to investigate if performances vary for different pointing angles. For this analysis, data sets for 45N and 90 pointing, of 493 and 361 passes respectively, corresponding to an observation window of 1 day (May 20, 2021), are used. This is the only case in which data sets differ from the one of 899 passes.

- *Interruption of detected signal, both for SNR and SR and DS*: this is simulated by randomly subtracting a certain percentage (10%, 20% and

50%) of measurements, such that, for those instants, the CM is built based on noise only. Signal interruption may occur for different reasons, such as the tumbling motion of the target or possible interference.

- *Larger channel bandwidth*: this is simulated by modifying the receiver channel bandwidth from 9 Hz to 50 Hz, 100 Hz, 1 kHz and 78 kHz. According to Eq. 19, this makes the signal less distinguishable from the noise. The channel bandwidth completely depends on the receiver back-end configuration and, so, this analysis aims at investigating the presence of related architectural constraints.

The second class includes scenarios that are expected to influence mainly the solution of the track ambiguity problem based on SNR criterion:

- *RCS fluctuations* (due to target tumbling, for instance): this is simulated by modifying the standard deviation of the measured SNR additional Gaussian noise from 0.5 dB to 1 dB, 2 dB and 5 dB, following an analogous analysis presented in [16].

- *Mismatching between the actual RCS and the one used to predict the SNR*: this is modeled by modifying the RCS adopted for the prediction from 1 m^2 to 0.1 m^2, 5 m^2 and 10 m^2. The RCS used to solve the ambiguity through SNR criterion is instead kept fixed to the nominal value of 1 m^2.

Focusing on the first class and referring to Tab. 3, it is possible to note that MATER performances are not altered by the pointing direction. On the contrary, Tab. 4 and Tab. 5 show that the algorithm accuracy (in terms of $\eta_{\Delta\gamma_1}$ and $\eta_{\Delta\gamma_2}$) deteriorates for increasing signal interruption rate and, moreover, receiver channel bandwidth. Indeed, focusing on the latter, synthetic CMs are built through the acquisition of the CW signal (Sec. 2) which is theoretically monochromatic. Consequently, larger bandwidths produce larger noise levels and, thus, more uncertain DOA estimations. This deteriorates the RANSAC based clustering process. Nevertheless, this deterioration is negligible, except when a 78 kHz bandwidth is considered: in this scenario, the failure rate increases significantly and the accuracy get much worse, producing a large mean correlation index $\overline{\zeta}$.
The results of the second class of scenarios are reported in Tab. 6 and Tab. 7. It is possible to appreciate that the SNR criterion is robust both to RCS fluctuations and mismatching. To recap, the sensitivity analysis shows that

Pointing [deg]	Success [%]	$\eta_{\Delta\gamma_1}$ [deg]	$\eta_{\Delta\gamma_2}$ [deg]	$\overline{\zeta}$
45 N	100	5.0e-04	4.6e-04	6.8e-02
90 N	100	2.8e-04	7.9e-04	1.3e-01

Table 3: Uncatalogued case: statistical analysis on synthetic data by considering different pointing direction.

Interruption [%]	Success [%]	$\eta_{\Delta\gamma_1}$ [deg]	$\eta_{\Delta\gamma_2}$ [deg]	$\overline{\zeta}$
10	100	1.2e-03	1.3e-03	6.8e-02
20	100	2.0e-03	1.8e-03	6.9e-02
50	100	4.0e-03	3.8e-03	8.0e-02

Table 4: Uncatalogued case: statistical analysis on synthetic data by varying the percentage of the pass in which no signal is detected.

MATER is quite robust to off-nominal conditions. In particular, SNR criterion with SR measurements confirms to be a reliable approach to solve the ambiguity problem. Major limitations may arise for large channel bandwidth, which may provide inaccurate DOA estimations.

6.3. Real signal

For the sake of completeness, the following analysis focuses on a test case in which the CMs are computed synthetically, while the SNR used to simulate the signal in Eq. 7 is derived from a real satellite pass. This analysis is conducted as an intermediate step between synthetic simulations and real observation. Similarly to the sensitivity analysis, this section deals with the uncatalogued case by applying the SNR criterion with SR measurements.

Bandwidth [Hz]	Success [%]	$\eta_{\Delta\gamma_1}$ [deg]	$\eta_{\Delta\gamma_2}$ [deg]	$\overline{\zeta}$
50	100	6.7e-04	4.5e-04	6.7e-02
100	100	8.1e-04	4.9e-04	6.8e-02
1e+03	100	2.4e-03	9.1e-04	7.3e-02
78e+03	72.2	2.5e-01	1.5e-01	2.7e+02

Table 5: Uncatalogued case: statistical analysis on synthetic data by varying the receiver channel bandwidth.

Fluctuations [dB]	Success [%]	$\eta_{\Delta\gamma_1}$ [deg]	$\eta_{\Delta\gamma_2}$ [deg]	$\overline{\zeta}$
1	100	5.2e-04	4.3e-04	6.8e-02
2	100	5.2e-04	4.7e-04	6.8e-02
5	100	5.6e-04	4.3e-04	6.8e-02

Table 6: Uncatalogued case: statistical analysis on synthetic data by varying the considered RCS fluctuations.

Actual RCS [m^2]	Success [%]	$\eta_{\Delta\gamma_1}$ [deg]	$\eta_{\Delta\gamma_2}$ [deg]	$\overline{\zeta}$
0.1	100	8.0e-04	4.9e-04	6.8e-02
5	100	4.7e-04	4.2e-04	6.8e-02
10	100	4.7e-04	4.2e-04	6.8e-02

Table 7: Uncatalogued case: statistical analysis on synthetic data by varying the actual RCS of the observed object. The RCS used in SNR criterion is kept fixed to the nominal value of 1 m^2.

The selected scenario is the re-entry of the Chinese launcher CZ-5B R/B occurred in May 2021. This reentry event was monitored by EUSST and BIRALES contributed to this observation campaign. In particular, the pass of May 5, 2021 at 02:18:53 a.m. (UTC), is here analyzed. The object was transiting southwards from the receiver, at an elevation of 37.1°. This was below the receiver minimum mechanical elevation of 42° (see Sec. 2) and so an electronic steering was exploited. The transmitter pointing was 40.8° in Azimuth and 42.1° in Elevation. This pass is selected because it is a real worst case scenario. Indeed, the object flies at low elevation with respect to the receiver and the signal exhibits strong variations and regularly repeating peaks due to the uncontrolled tumbling motion of the target. The recorded signal is reported in Fig. 18. Overall, about 58.2 % of the pass produce no SNR, which is more than the worst case scenario analyzed in the previous section.

This varying signal produces frequent failures in the DOA estimation, as illustrated in Fig. 19, which shows the output of the track estimation phase. Since the pointing was southwards, the object moves from right (positive $\Delta\gamma_1$) to left (negative $\Delta\gamma_1$). It is possible to note that the estimates are spread over the entire FoV, except for those instants corresponding to a high intensity signal. Then, the track refinement phase is performed: the

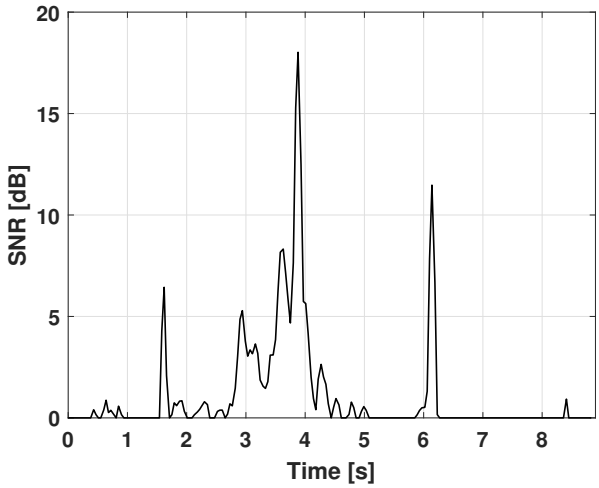


Figure 18: Real SNR profile of the CZ-5B R/B pass observed by BIRALES on the 5^{th} of May 2021. The strongly varying signal and the regularly repeating peaks are due to the uncontrolled tumbling motion of the target.

DOAs are clustered, their regression is performed and the SNR criterion with SR measurements is applied. In this way, MATER provides the track reported in Fig. 20, together with the correct DOAs identified by solving the ambiguity and then used for the final regression. Its performance indexes are listed in Tab. 8. It is possible to note that there is a deterioration in track reconstruction accuracy with respect to the simulated scenarios. This is strictly due to the noisy DOA estimates (which then affect the RANSAC based clustering process). Yet, especially considering the relevant noise of the SNR measurements, MATER provides a reasonably accurate track estimate.

$\eta_{\Delta\gamma_1}$ [deg]	$\eta_{\Delta\gamma_2}$ [deg]	$\overline{\zeta}$
4.5e-02	1.3e-02	2.2e-01

Table 8: Real SNR profile of the CZ-5B R/B pass observed by BIRALES on the 5^{th} of May 2021: performance.

7. Real observation

In this section, MATER performance is assessed on a real observation.

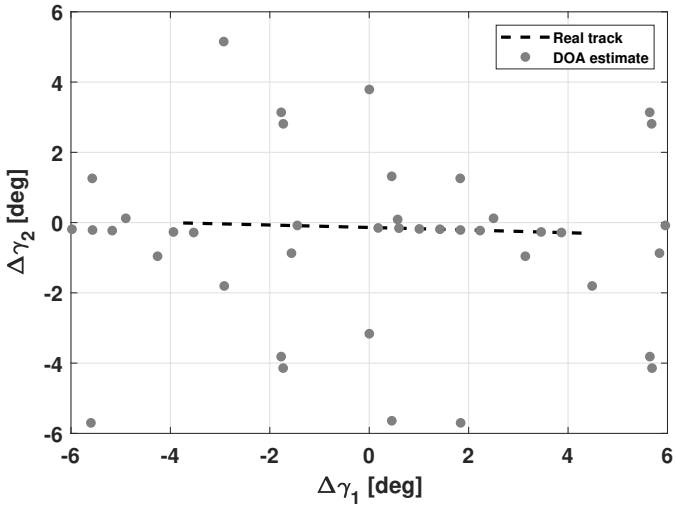


Figure 19: Real SNR profile of the CZ-5B R/B pass observed by BIRALES on the 5^{th} of May 2021: track estimation result.

The algorithm could only be run using the current receiver back-end of BIRALES, which does not match exactly the typical requirements for optimal MATER performance, as those analysed in the previous sections. In particular, two aspects of the current system yield relevant drawbacks: the CM integration time and the receiver channel bandwidth. Concerning the former, in a LEO satellite observation, the source (and consequently the DOA) moves relatively fast in the receiver FoV. Thus, the CM should be constructed with a relatively short integration time. Regarding the channel bandwidth instead, the sensitivity analysis of Sec. 6 shows that there is a performance deterioration when it is too large with respect to the detected signal bandwidth. Considering that the continuous wave signal reflected by the object is ideally monochromatic, the receiver channel bandwidth should be relatively narrow, since the larger the receiver bandwidth is, the more the SNR is attenuated.
BIRALES is currently configured to use the multibeam strategy described in Sec. 2. The corresponding settings prevented an optimal generation of the real CMs. On one hand, the CM integration time was 0.42 s, which introduces a significant uncertainty on the estimated DOA. On the other hand, the CM can only be built on a signal acquired with a channel with 78 kHz bandwidth (the worst case bandwidth scenario analyzed in Sec. 6). This limitation poses a severe constraint, as the current BIRALES back-end allows

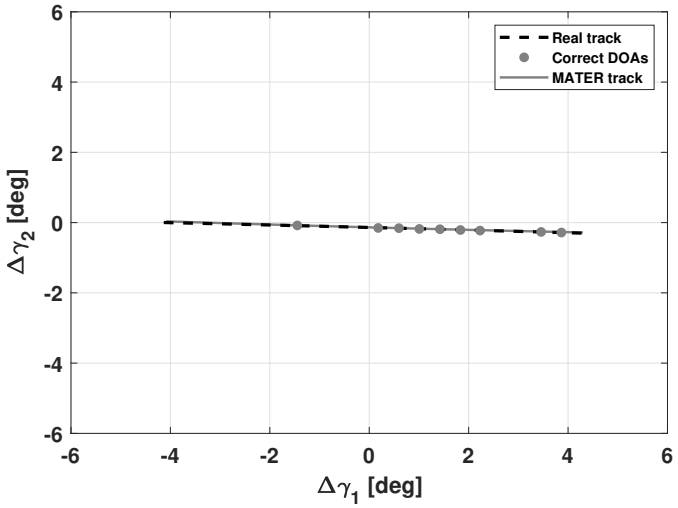


Figure 20: Real SNR profile of the CZ-5B R/B pass observed by BIRALES on the 5^{th} of May 2021: track refinement result, represented together with the correct DOAs used for the final regression.

MATER to be realistically applied only on the observation of resident space objects providing a relatively intense received signal (i.e., large RCS and/or low slant range). For this reason, the results obtained on the observation of the International Space Station (ISS) are reported hereafter. The observed pass occurred on April 28, 2021 at 08:44:32 (UTC), southwards from the receiver, at an elevation of 83.9°. The transmitter pointing angles were 19.3° in Azimuth and 35.1° in Elevation.
The resulting MUSIC pattern, for a generic instant, is illustrated in Fig. 21, where it is possible to appreciate the presence of multiple peaks, similarly to Fig. 5. The DOAs resulting from the track estimate phase are reported in Fig. 22, while the reconstructed angular profile after the track refinement phase (in which the OD criterion based on SR is used) is reported in Fig. 23, together with the correct DOAs (identified by solving the ambiguity) used to obtain the final regression. The estimated DOAs are along the real track for a large portion of the pass. Yet, a slight time shift between the real track and the one estimated by MATER can be observed (e.g., close to the end points of the track). This shift can be mainly attributed to four possible factors: the relatively long CM integration time and the associated time uncertainty introduced in the estimated DOA, the signal quality (attenuated by the 78 kHz channel bandwidth), the inaccuracy of the reference ISS track (which

has been retrieved from TLE) the result is compared to and, possibly, sensor calibration inaccuracies. All of these factors have an impact on the performances reported in Tab. 9 (for the uncatalogued case): the angular RMSEs are about 2 order of magnitude larger than those obtained with the statistical analysis presented in Sec. 6; also the correlation index is quite inaccurate. Nevertheless, the results are encouraging as they show that MATER algorithm can reconstruct the track for orbit determination purposes, even when a not optimal back-end is used, as in the current settings.

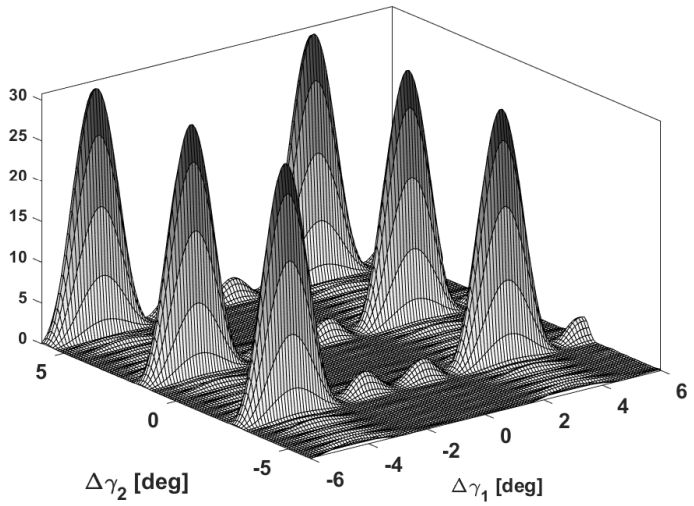


Figure 21: Real pass of the International Space Station (ISS) on April 28, 2021 at 08:44:32 (UTC): 3D array response.

$\eta_{\Delta\gamma_1}$ [deg]	$\eta_{\Delta\gamma_2}$ [deg]	$\overline{\zeta}$
1.5e-01	9.2e-02	2.0e-01

Table 9: Real pass of the International Space Station (ISS) on April 28, 2021 at 08:44:32 (UTC): performance.

8. Conclusions

A method to estimate the angular track of resident space objects in the sensor FoV of the multireceiver radar BIRALES has been proposed. The

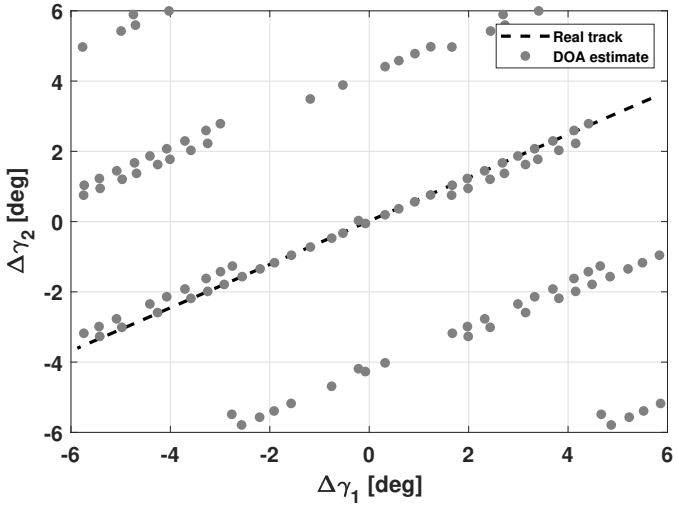


Figure 22: Real pass of the International Space Station (ISS) on April 28, 2021 at 08:44:32 (UTC): track estimate.

measurements are processed in two steps: first, the signal DOA is estimated using MUSIC algorithm; then intrinsic solution ambiguity due to array geometry is solved to derive a unique time dependent angular profile. Depending on the available measurements, different approaches to solve the ambiguity have been presented and tested.

A statistical analysis performed on simulated measurements shows that the overall process is reliable and robust. The performance deteriorates when the method is applied to a real observation of the ISS. However, this observation was affected by the limitations of the current BIRALES back-end, which cannot optimally generate the CMs for DOA estimation.

Nevertheless, the results are deemed to be encouraging: a proper modification of the current back-end is expected to provide a much higher accuracy. Consequently, future work will be devoted to the upgrade of the receiver back-end to meet the MATER requirements, especially in terms of CM integration time and channel bandwidth. This upgrade will trigger the possibility of performing a more extensive analysis of real data to achieve a more robust assessment of MATER performance.

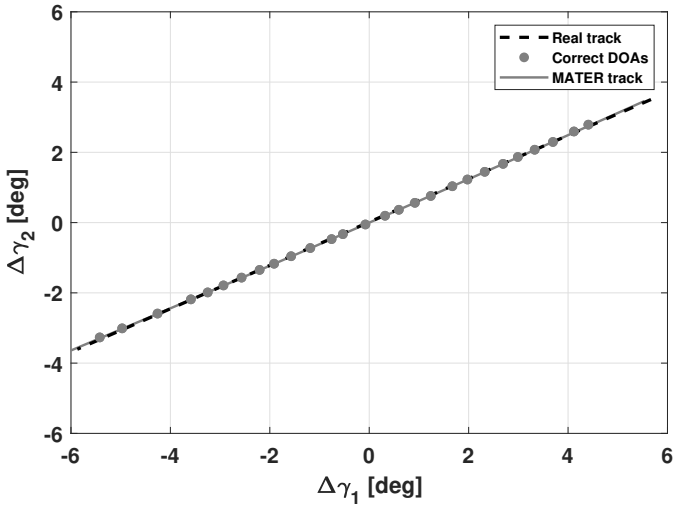


Figure 23: Real pass of the International Space Station (ISS) on April 28, 2021 at 08:44:32 (UTC): track refinement result, represented together with the correct DOAs used for the final regression.

9. Acknowledgement

The research activities described in this paper were performed within the European Commission Framework Programme H2020 and Copernicus "SST Space Surveillance and Tracking" contracts N. 952852 (2-3SST2018-20) and N. 237/G/GRO/COPE/16/8935 (1SST2018-20) with further support from the Italian Space Agency through the grant agreement n. 2020-6-HH.0 (Detriti Spaziali – Supporto alle attivit'a IADC e SST 2019-2021).

The authors are grateful to Delphine Cerutti-Maori for the interesting and fruitful discussions on the topic, which eventually inspired this work.

References

[1] Space debris by the numbers, European Space Agency, accessed 11.04.2022.
URL https://www.esa.int/Our_Activities/Operations/Space_Safety_Security/Space_Debris/Space_debris_by_the_numbers

[2] Inter-Agency Space Debris Coordination committee, Space Debris Mitigation Guidelines (2002).

[3] Cnes space debris website, Centre national d'études spatiales, accessed 11.04.2022.
URL https://debris-spatiaux.cnes.fr/fr/risques-en-orbite

[4] Consultative Committee for Space Data Systems, CCSDS 508.0-B-1, Conjunction Data Message (2013).

[5] Space fence, United States Space Force, accessed 11.04.2022.
URL https://en.wikipedia.org/wiki/Space_Fence

[6] Eusst website, European Space Surveillance and Tracking, accessed 11.04.2022.
URL https://www.eusst.eu/about-us/

[7] D. Cerutti-Maori, et al., A novel high-precision observation mode for the tracking and imaging radar tira – principle and performance evaluation, in: in Proc. 8th European Conference on Space Debris, 2021.

[8] A. Jouadé, A. Barka, Massively parallel implementation of feti-2lm methods for the simulation of the sparse receiving array evolution of the graves radar system for space surveillance and tracking, IEEE Access 7 (2019) 128968–128979. doi:10.1109/ACCESS.2019.2938011.

[9] F. Muller, Graves space surveillance system: Life extension and upgrade program, in: in Proc. 7th European Conference on Space Debris, 2017.

[10] R. Casado Gomez, et al., Initial operations of the breakthrough spanish space surveillance and tracking radar (s3tsr) in the european context, in: in Proc. st NEO and Debris Detection Conference, 2019.

[11] H. Wilden, N. Ben Bekhti, R. Hoffmann, C. Kirchner, R. Kohlleppel, C. Reising, A. Brenner, T. Eversberg, Gestra - recent progress, mode design and signal processing, in: 2019 IEEE International Symposium on Phased Array System Technology (PAST), 2019, pp. 1–8. doi:10.1109/PAST43306.2019.9020744.

[12] DLR, GESTRA - German Experimental Space Surveillance and Tracking Radar, 58 th session of the Scientific and Technical Subcommittee of UNCOPUOS (2021).

[13] H. Wilden, et al., Gestra - technology aspects and mode design for space surveillance and tracking, in: in Proc. 7th European Conference on Space Debris, 2017.

[14] T. Pisanu, L. Schirru, E. Urru, F. Gaudiomonte, P. Ortu, G. Bianchi, C. Bortolotti, M. Roma, G. Muntoni, G. Montisci, F. Protopapa, A. Podda, A. Sulis, G. Valente, Upgrading the italian birales system to a pulse compression radar for space debris range measurements, in: 2018 22nd International Microwave and Radar Conference (MIKON), 2018, pp. 317–320. doi:10.23919/MIKON.2018.8405212.

[15] G. Bianchi, C. Bortolotti, M. Roma, G. Pupillo, G. Naldi, L. Lama, F. Perini, M. Schiaffino, A. Maccaferri, A. Mattana, A. Podda, S. Casu, F. Protopapa, A. Coppola, P. Di Lizia, G. Purpura, M. Massari, M. F. Montaruli, T. Pisanu, L. Schirru, E. Urru, Exploration of an innovative ranging method for bi-static radar, applied in leo space debris surveying and tracking, in: Proceedings of the International Astronautical Congress, IAC, Vol. 2020-October, 2020, cited By :1.
URL www.scopus.com

[16] M. Losacco, P. Di Lizia, M. Massari, G. Naldi, G. Pupillo, G. Bianchi, J. Siminski, Initial orbit determination with the multi-beam radar sensor birales, Acta Astronautica 167 (2020) 374–390. doi:https://doi.org/10.1016/j.actaastro.2019.10.043.
URL https://www.sciencedirect.com/science/article/pii/S0094576519313712

[17] Consultative Committee for Space Data Systems, CCSDS 503.0-B-2, Tracking Data Message (2020).

[18] B. D. Tapley, B. E. Schutz, G. Born, Statistical Orbit Determination, Elsevier Academic Press, 2004.

[19] J. Siminski, Techniques for assessing space object cataloguing performance during design of surveillance systems, in: in Proc. 6th International Conference on Astrodynamics Tools and Techniques (ICATT), 2016.

[20] S. Julier, J. Uhlmann, Unscented filtering and nonlinear estimation, Proceedings of the IEEE 92 (3) (2004) 401–422. doi:10.1109/JPROC.2003.823141.

[21] Navigation Data Messages Overview, CCSDS 500.2-G-2 (2020).

[22] C. Yanez, F. Mercier, J. C. Dolado, A novel initial orbit determination algorithm from doppler and angular information, in: in Proc. 7th Conference on Space Debris, 2017.

[23] G. F. Masters, S. F. Gregson, Coordinate system plotting for antenna measurements, 2007.

[24] H. L. Van Trees, Optimum Array Processing, John Wiley & Sons, 2002.

[25] R. O. Schmidt, A signal subspace approach to multiple emitter location and spectral estimation, Stanford University, 1981.